4

Gradient-based approach for determination of oscillating flow fields in PIV

Atsushi Nomura, Koichi Okada and Hidetoshi Miike
Yamaguchi University
Japan

Hidemi Yamada
Oita University
Japan

1. Introduction

Oscillating velocity vector fields are often observed in fluid flow fields. A flow field caused by the Karman vortices is a typical example of an oscillating velocity vector field. In particle image velocimetry (PIV), a velocity vector field is determined from an image sequence representing a fluid flow field visualised by particles (Adrian, 1991; Raffel et al., 2007). When we focus on an oscillating velocity vector field, we can expect that the oscillatory characteristic of the field is useful for determining a high accurate velocity vector field. Thus, utilising the oscillatory characteristic as an additional constraint is an interesting topic for the PIV approaches, such as the matching-based approach and the gradient-based one.

The matching-based approach utilises a pattern-matching procedure, which calculates a cross-correlation function between two image templates on the two successive image frames. The peak position of the obtained two-dimensional cross-correlation function provides a displacement vector for a brightness pattern during one frame, that is, a velocity vector. Under the low density of particles, it is possible to track a particular particle during two or more successive image frames by the pattern-matching procedure (Hassan et al., 1992). When the density of particles is in the middle range, the pattern-matching procedure for a particle distribution function is utilised to detect its velocity vector (Willert and Gharib, 1991).

The gradient-based approach first estimates spatio-temporal gradients on an image brightness function, and then derives the basic constraint equation consisting of the gradients and two velocity components (Horn and Schunck, 1981). The basic constraint equation is derived from the correspondence of a moving image brightness pattern during a short time period. Next, it organises the error function consisting of the basic constraint equation and additional one(s) modelling the characteristics of a fluid flow field. Finally, minimising the error function by an optimisation method provides the two velocity components.

There are several problems in the matching-based approach and the gradient-based one. With the gradient-based approach, it is difficult to determine high speed flow fields. In contrast to this, while the matching-based approach can determine such the high speed flow fields, the sub-pixel accuracy of the approach is generally unreliable. The gradient-based approach

provides the high resolution of velocity vector fields, namely, dense velocity vector fields. Both the approaches have difficulty in determining high velocity gradients.
To overcome these problems in the particular approaches, several methods have been proposed. The multigrid relaxation method enlarges the velocity range of the gradient-based approach (Terzopoulos, 1986). Sub-pixel peak detection techniques for the cross-correlation function improve the sub-pixel accuracy on determined velocity vectors in the matching-based approach (Roesgen, 2003). The hybrid method consisting of the gradient-based approach and the matching-based one achieves the large velocity range and the reliable sub-pixel accuracy (Sugii et al, 2000). The combination of the matching procedure on a particle distribution and the tracking procedure on a particular particle provides the high resolution on a velocity vector field (Cowen and Monismith, 1997). Tokumaru and Dimotakis (1995) proposed a matching-based method that improves the accuracy of the velocity vector field having high velocity gradients. Their method expresses a local velocity vector field with the Taylor series including higher order velocity gradients. The method organises the error function expressing the Lagrangian invariance on a moving brightness pattern as well as a spatial smoothness constraint on velocity. The method minimises the error function by the global optimisation strategy utilised in the gradient-based method of Horn and Schunck (1981). Several researchers also proposed to adaptively shift and distort image templates and a search area for the pattern matching procedure according to previously determined velocity vector fields, by utilising the iterative, interpolating and multigrid techniques (Westerweel et al., 1997; Fincham and Delerce, 2000). Scarano (2002) reviewed the matching-based approach with adaptive templates; the approach has been developed intensively as a state-of-the-art one (Astarita, 2009; Theunissen et al., 2010). Hart (2000) and Meinhart et al. (2000) proposed the methods utilising multiple cross-correlation functions to obtain a reliable cross-correlation function. In particular, concerning the present topic of determination of oscillating flow fields, the method proposed by Meinhart et al. (2000) averages multiple cross-correlation functions obtained for a stationary or oscillatory flow field and searches the maximum peak position from the obtained reliable cross-correlation function.
This chapter proposes two gradient-based methods which focus on temporally oscillating velocity vector fields for achieving high accuracy and high spatio-temporal resolution. Previous studies on the gradient-based approach present no methods focusing on oscillating velocity vector fields. The two methods proposed here utilise the oscillatory characteristic as additional constraints. A fixed velocity vector field regularly appears at the time intervals of its oscillation period. Thus, a constancy assumption on velocity is applicable to basic constraint equations sampled at the time intervals. One of the proposed methods utilises the constancy assumption for the sampled basic constraint equations as an additional constraint. The other method assumes that the temporal change of a velocity vector at a fixed pixel site is approximately expressed by the Fourier series. Thus, the method utilises the Fourier series as an additional constraint. The preliminary knowledge of the oscillatory characteristic of a fluid flow field helps to improve the accuracy and the temporal resolution of the approach.
To realise the two methods utilising the proposed constraints, it is necessary to determine the oscillation period in advance. This chapter proposes two methods for determining the oscillation period. One of the methods tentatively determines velocity vectors by an ordinary gradient-based method which requires little calculation cost, and then analyses the temporal changes of the tentative velocity vectors by the Fourier analysis method. An obtained power spectrum distribution provides the oscillation period. The other method first analyses spatio-temporal sectional images by a spatio-temporal filter. The spatio-temporal sectional images

are sliced from an original image sequence; the filter detects the direction of a short line segment representing a particle trajectory on a spatio-temporal sectional image. The outputs of the filter are also analysed by the Fourier analysis method along a time coordinate system.
The proposed two gradient-based methods are quantitatively compared to ordinary gradient- and matching-based methods through the analysis of synthetic image sequences. The ordinary gradient-based method utilises a simple phase-averaging processing method as post-processing; the ordinary matching-based method utilises an averaged version of the cross-correlation function proposed by Meinhart et al. (2000). Experimental results for the synthetic image sequences show the characteristics of the proposed methods and the ordinary ones. Finally, we apply the proposed two gradient-based methods and the ordinary ones to a real image sequence of the Karman vortices.

2. Background

2.1 Matching-Based Approach: Average Correlation Method

An ordinary matching-based approach determines a velocity vector by seeking the correspondence of a moving brightness pattern between two successive image frames $f(x, y, t)$ and $f(x, y, t+1)$ by the use of a cross-correlation function $C_{t,t+1}(d_x, d_y)$ (e.g., Raffel et al., 2007). The function $C_{t,t+1}(d_x, d_y)$ evaluates similarity between two image templates, one of which has its centre at the pixel site (x, y) on the tth image frame and the other of which has its centre at the pixel site $(x + d_x, y + d_y)$ on the $(t+1)$th image frame. Both the templates have the $(2L_x + 1) \times (2L_y + 1)$ (pixels^2) rectangular domains surrounding their centre pixel sites.
For the determination of oscillating flow fields or stationary ones with high accuracy, Meinhart et al. (2000) proposed to utilise the averaged version of the cross-correlation function in the matching-based approach. Their method calculates the averaged cross-correlation function $C_a(d_x, d_y)$ from cross-correlation functions obtained at the time intervals of the oscillation period T, that is, at $t, t + [T], t + [2T], \cdots t + [(K-1)T]$ (frame), and/or within the temporal local domain $(2L_t + 1)$ (frames),

$$C_a(d_x, d_y) = \frac{1}{K \times (2L_t + 1)} \sum_{k=0}^{K-1} \sum_{t_0=t+[kT]-L_t}^{t+[kT]+L_t} C_{t_0,t_0+1}(d_x, d_y), \tag{1}$$

where the symbol $[\cdot]$ refers to the Gauss' notation. By changing the discrete displacement parameters d_x and d_y in the ranges of $-W_x \leq d_x \leq W_x$ and $-W_y \leq d_y \leq W_y$ (pixels), we obtain the averaged cross-correlation function C_a defined within the rectangular domain consisting of $(2W_x + 1) \times (2W_y + 1)$ (pixels^2). The peak position of the averaged cross-correlation function provides the discrete displacement vector (d_{x_0}, d_{y_0}) at the position (x, y) and at the tth frame. The method utilising the averaged version of Eq. (1) is called the "Average Correlation Method (ACM)".
For sub-pixel accuracy on a velocity vector, an ordinary matching-based method fits the Gaussian function to the cross-correlation function around its peak position (d_{x_0}, d_{y_0}). Let us utilise the peak position and its neighbouring four discrete positions $(d_{x_0} - 1, d_{y_0})$, $(d_{x_0} + 1, d_{y_0})$, $(d_{x_0}, d_{y_0} - 1)$ and $(d_{x_0}, d_{y_0} + 1)$. Then, we fit the five points and their corresponding averaged cross-correlation values,

$$C_{a_{,}} = C_a(d_{x_0}, d_{y_0}), \quad C_{a_{-,}} = C_a(d_{x_0} - 1, d_{y_0}), \quad C_{a_{+,}} = C_a(d_{x_0} + 1, d_{y_0}),$$
$$C_{a_{,-}} = C_a(d_{x_0}, d_{y_0} - 1), \quad C_{a_{,+}} = C_a(d_{x_0}, d_{y_0} + 1),$$

to the following two-dimensional Gaussian function having the peak value C_m, the sub-pixel peak position $(d^*_{x_0}, d^*_{y_0})$ and the variances (k_x^2, k_y^2),

$$C_a(d_x, d_y) = C_m \exp\left(-\frac{(d_x - d^*_{x_0})^2}{k_x^2} - \frac{(d_y - d^*_{y_0})^2}{k_y^2}\right). \tag{2}$$

Finally, we obtain the two velocity components with the sub-pixel accuracy,

$$\begin{aligned} u(x,y,t) = d^*_{x_0} &= d_{x_0} + (\ln C_{a_{-,}} - \ln C_{a_{+,}})/(2\ln C_{a_{-,}} - 4\ln C_{a,} + 2\ln C_{a_{+,}}), \\ v(x,y,t) = d^*_{y_0} &= d_{y_0} + (\ln C_{a,-} - \ln C_{a,+})/(2\ln C_{a,-} - 4\ln C_{a,} + 2\ln C_{a,+}), \end{aligned} \tag{3}$$

as well as the other parameters of,

$$k_x^2 = \{2(d^*_{x_0} - d_{x_0}) + 1\}/(\ln C_{a,} - \ln C_{a_{-,}}),\ k_y^2 = \{2(d^*_{y_0} - d_{y_0}) + 1\}/(\ln C_{a,} - \ln C_{a,-}), \tag{4}$$

and

$$C_m = C_{a,} \exp\left(\frac{(d^*_{x_0} - d_{x_0})^2}{k_x^2} + \frac{(d^*_{y_0} - d_{y_0})^2}{k_y^2}\right). \tag{5}$$

2.2 Gradient-Based Approach: Local Optimisation Method

The gradient-based approach utilises the following basic constraint equation,

$$f_x u + f_y v + f_t = 0 \tag{6}$$

where f_x, f_y, f_t are spatio-temporal gradients on the brightness distribution function $f(x,y,t)$ of an image sequence, and $\vec{v} = (u,v)$ is the set of two velocity components to be determined. Equation (6) is derived from a correspondence relation on a moving rigid brightness pattern during a short time period (Horn and Schunck, 1981). The spatio-temporal gradients are numerically estimated for the brightness distribution function.

It is not able to determine the set of the two unknown components (u,v) with one constraint of Eq. (6) at a particular pixel site (x,y,t). One more additional constraint is necessary for the determination of the velocity components. A very simple assumption that two neighbouring pixel sites, such as (x,y,t) and $(x,y,t+1)$, have the same velocity (u,v), brings the following two basic constraint equations sharing the two unknowns (u,v).

$$\begin{aligned} f_x(x,y,t)u + f_y(x,y,t)v + f_t(x,y,t) &= 0 \\ f_x(x,y,t+1)u + f_y(x,y,t+1)v + f_t(x,y,t+1) &= 0 \end{aligned} \tag{7}$$

Solving the set of the two equations for the two unknown parameters (u,v) provides the velocity vector.

For obtaining more stable solution, which is robust to the random noise component contained in realistic image sequences, Kearney et al. (1987) proposed a constancy assumption on a velocity vector field within a spatial local domain as an additional constraint. We proposed a temporal constancy assumption on a velocity vector field during a temporal local domain (Nomura et al., 1991). More generally, we can assume that a velocity vector field is constant within a spatio-temporal local domain $\delta S \times \delta T$.

$$\vec{v}(x,y,t) \ \text{ is constant in } \ \delta S \times \delta T. \tag{8}$$

Equation (8) assumes that the basic constraint equations derived within the local domain $\delta S \times \delta T$ share the same velocity components. Thus, we organise the following error function with the basic constraint equations derived within the domain $\delta S \times \delta T$; the error function defines the sum of the departure values of the basic constraint equations from zero under the spatio-temporal constancy assumption of Eq. (8) (Nakajima et al., 1997),

$$E(u,v) = \frac{1}{2} \sum_{\delta S \times \delta T} \left(f_x u + f_y v + f_t \right)^2 \rightarrow \text{minimum}, \tag{9}$$

where the gradients f_x, f_y, f_t are estimated at a particular pixel site (x, y, t) within the spatio-temporal domain $\delta S \times \delta T$ consisting of $(2L_x + 1) \times (2L_y + 1)$ (pixels^2) and $(2L_t + 1)$ (frames). By minimising the error function of Eq. (9) with $\partial E/\partial u = 0$ and with $\partial E/\partial v = 0$, we obtain the next set of linear equations,

$$\begin{pmatrix} \sum f_x^2 & \sum f_x f_y \\ \sum f_x f_y & \sum f_y^2 \end{pmatrix} \begin{pmatrix} u \\ v \end{pmatrix} = - \begin{pmatrix} \sum f_x f_t \\ \sum f_y f_t \end{pmatrix}, \tag{10}$$

where the symbol $\sum$ refers to the summation within the domain $\delta S \times \delta T$. This method assuming the spatio-temporal local constancy on a velocity vector field is called the "Local Optimisation Method (LOM)" (Kearney et al., 1987).
Many other additional constraints have been proposed. Horn and Schunck (1981) proposed a spatial smoothness constraint on a velocity vector field. Nakajima et al. (2003) proposed the additional constraints consisting of the continuity equation and the Navier-Stokes ones for determining a fluid flow field. Corpetti et al. (2002) proposed an additional constraint designed for preserving a rotational field and a divergent one on a fluid flow field.
The basic constraint Eq. (6) requires the estimation of spatio-temporal gradients f_x, f_y, f_t. For example, the gradient $f_x(x, y, t)$ is approximately estimated by the forward difference method at a point $(x + 1/2, y + 1/2, t + 1/2)$ as follows.

$$\begin{aligned} f_x(x,y,t) \simeq \frac{1}{4} \{ & f(x+1,y,t) - f(x,y,t) + f(x+1,y+1,t) - f(x,y+1,t) \\ & + f(x+1,y,t+1) - f(x,y,t+1) + f(x+1,y+1,t+1) - f(x,y+1,t+1) \} \end{aligned} \tag{11}$$

The above Eq. (11) estimates the gradient f_x averaged for the four pairs of the forward differences within 2×2 (pixels^2) and 2 (frames). In addition, by averaging the gradient f_x over more global spatial domain consisting of $(2L_a + 1) \times (2L_a + 1)$ (pixels^2), we can expect the reliable gradient $\overline{f_x}$.

$$\overline{f_x}(x,y,t) \simeq \frac{1}{(2L_a+1)^2} \sum_{y_0=y-L_a}^{y+L_a} \sum_{x_0=x-L_a}^{x+L_a} f_x(x_0, y_0, t) \tag{12}$$

The other gradients $\overline{f_y}$ and $\overline{f_t}$ are also estimated in the same way.

3. Proposed Method in the Gradient-Based Approach

3.1 Additional constraints for oscillating flow fields

We propose two additional constraints to determine an oscillating velocity vector field. Let us fix an observation point at a pixel site (x, y) on an image plane, and observe the temporal

change of a velocity vector field. When the velocity vector field is oscillating with time t, a fixed velocity vector $\vec{v} = (u, v)$ regularly appears at the intervals of its oscillation period T,

$$\vec{v}(x, y, t + kT) \text{ is constant for } k = 0, 1, \cdots, K-1, \tag{13}$$

where the oscillation period T is constant from the time t to $t + (K-1)T$ at the pixel site (x, y). The parameter K refers to the number of multiple periods contained in the frame number $S_t = KT$ (frames). (In general, the parameter 'K' refers to the wave number of $1/T$, that is, the number of multiple periods per unit time. However, in this chapter, the parameter K refers to the number of multiple periods contained in the whole image frames or the temporal length S_t of an image sequence utilised for velocity determination.) Equation (13) is the first additional constraint proposed in this chapter. Basic constraint equations sampled at the time intervals of T share the same velocity vector $\vec{v} = (u, v)$. Thus, if we preliminarily know the parameter T and if we also assume the spatio-temporal local constancy on the velocity vector field within the spatio-temporal domain $\delta S \times \delta T$, we can determine two velocity components by minimising the next error function,

$$E(u, v) = \frac{1}{2} \sum_{k=0}^{K-1} \sum_{\delta S \times \delta T} \left(f_x u + f_y v + f_t \right)^2 \rightarrow \text{minimum}, \tag{14}$$

where the gradients f_x, f_y, f_t are estimated at $(x, y, t + kT)$; the pixel site (x, y, t) is in $\delta S \times \delta T$ consisting of $(2L_x + 1) \times (2L_y + 1)$ (pixels^2) and $(2L_t + 1)$ (frames). In computing Eq. (14), the gradients are estimated at the nearest pixel site, that is, at $(x, y, t + [kT + 1/2])$. By minimising the error function of Eq. (14), we obtain the set of linear equations similar to Eq. (10). We can recognise that the additional constraint of Eq. (13) works as a kind of phase-averaging in the method of Eq. (14). Later, we propose two methods to determine the oscillation period T and the number of multiple periods K from an image sequence.

The second additional constraint proposed here assumes that the oscillating velocity components can be expanded into the Fourier series with the Mth highest harmonics as follows,

$$u = u_0 + \sum_{m=1}^{M} \left(a_m \sin \frac{2\pi m t}{T} + b_m \cos \frac{2\pi m t}{T} \right), \tag{15}$$

$$v = v_0 + \sum_{m=1}^{M} \left(c_m \sin \frac{2\pi m t}{T} + d_m \cos \frac{2\pi m t}{T} \right), \tag{16}$$

where the parameters u_0 and v_0 are the direct components of the velocity vector along a time coordinate system t; the parameters a_m, b_m, c_m, d_m are the amplitude coefficients of the mth harmonics. We define the next error function and substitute the additional constraint of Eqs. (15) and (16) for the two velocity components u and v of the next error function,

$$E(u_0, a_m, b_m, v_0, c_m, d_m) = \frac{1}{2} \sum_{t=0}^{S_t - 1} \sum_{\delta S} \left(f_x u + f_y v + f_t \right)^2 \rightarrow \text{minimum}, \tag{17}$$

where the parameters $u_0, v_0, a_m, b_m, c_m, d_m$ for $m = 1, 2, \cdots, M$ are constants in the spatial local domain δS and during the whole image frames S_t; the gradients f_x, f_y, f_t are estimated at a

particular pixel site within the spatial local domain δS and during the whole image frames S_t. By minimising the error function of Eq. (17), we obtain the following set of linear equations,

$$\begin{aligned}
\frac{\partial E}{\partial u_0} &= \sum_{t=0}^{S_t-1}\sum_{\delta S} E_d f_x = 0, & \frac{\partial E}{\partial v_0} &= \sum_{t=0}^{S_t-1}\sum_{\delta S} E_d f_y = 0,\\
\frac{\partial E}{\partial a_n} &= \sum_{t=0}^{S_t-1}\sum_{\delta S} E_d f_x \sin\frac{2\pi nt}{T} = 0, & \frac{\partial E}{\partial b_n} &= \sum_{t=0}^{S_t-1}\sum_{\delta S} E_d f_x \cos\frac{2\pi nt}{T} = 0,\\
\frac{\partial E}{\partial c_n} &= \sum_{t=0}^{S_t-1}\sum_{\delta S} E_d f_y \sin\frac{2\pi nt}{T} = 0, & \frac{\partial E}{\partial d_n} &= \sum_{t=0}^{S_t-1}\sum_{\delta S} E_d f_y \cos\frac{2\pi nt}{T} = 0,
\end{aligned} \tag{18}$$

where $n = 1, 2, \cdots, M$ and E_d refers to the departure value of the basic constraint Eq. (6) combined with the additional constraint of Eqs. (15) and (16) from zero as follows,

$$\begin{aligned}
E_d = f_t + f_x &\left\{ u_0 + \sum_{m=1}^{M}\left(a_m \sin\frac{2\pi mt}{T} + b_m \cos\frac{2\pi mt}{T}\right)\right\}\\
&+ f_y \left\{ v_0 + \sum_{m=1}^{M}\left(c_m \sin\frac{2\pi mt}{T} + d_m \cos\frac{2\pi mt}{T}\right)\right\}.
\end{aligned} \tag{19}$$

Note that the number of unknown parameters is $(2+4M)$. Thus, the number of pixel sites $(2L_x+1)\times(2L_y+1)\times S_t$ utilised for velocity determination should be larger than $(2+4M)$. The singular value decomposition is applied to the coefficient matrix of the set of linear equations derived from Eqs. (18) and (19). A singular value obtained by the decomposition is referred as S_i for the subscript index $i = 0, 1, 2, \cdots, (2+4M)-1$. When a singular value S_i is smaller than $\beta \max_i(S_i)$, the singular value is rejected and the inverse $1/S_i$ is replaced with zero in solving the set of linear equations (Press et al., 1988). The parameter β refers to the ratio between the maximum singular value and the threshold one; the parameter is usually set to a quite small value $0 < \beta \ll 1$. The singular value decomposition provides the set of solutions $(u_0, a_1, b_1, \cdots, a_M, b_M, v_0, c_1, d_1, \cdots, c_M, d_M)$.

3.2 Determining an oscillation period and the number of multiple periods

The above proposed additional constraints require the oscillation period T and the number of multiple periods K to organise the error functions of Eq. (14) and Eq. (17). Several approaches are possible for determining T and K. One of the approaches first determines tentative time-varying velocity vector fields by a simple ordinary gradient-based method solving Eq. (7) or Eq. (10), and then analyses temporal changes of the tentatively determined velocity vectors by the Fourier analysis method. The maximum peak position of the power spectrum distribution function obtained by the Fourier analysis method provides the oscillation period T and the number K.

Another method for determining the oscillation period T and the number K utilises a spatio-temporal sectional image. Let us assume that the vertical component v of a velocity vector is oscillating with time t, and that the other horizontal component u is zero. A particle moves at an oscillating velocity vector. A spatio-temporal sectional image with a $y-t$ plane contains the trajectory of the moving particle; the trajectory becomes a sinusoidal pattern [Fig. 1(a)]. A filter that detects the direction of a short line segment on the spatio-temporal sectional image provides a one-dimensional oscillatory signal along the time coordinate system. Figure 1(b)

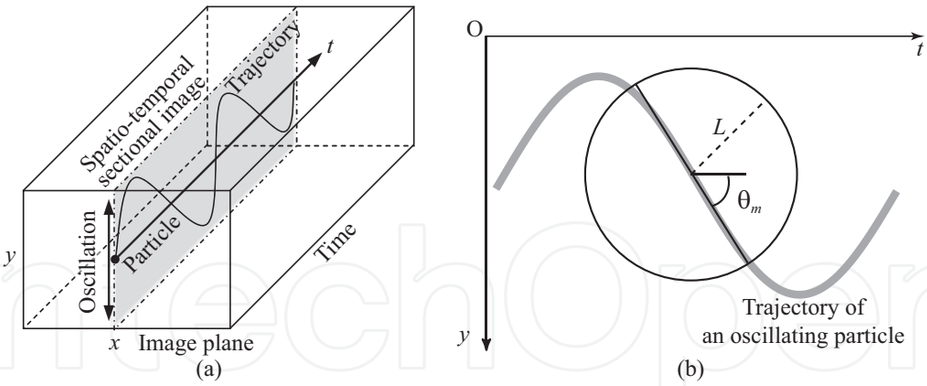

Fig. 1. Oscillation of a visualisation particle. (a) Spatio-temporal sectional image sliced from an image sequence, which contains an oscillating particle on a $y-t$ plane. The trajectory of the particle illustrates a sinusoidal pattern on the spatio-temporal sectional image. (b) Spatio-temporal filter detecting the direction of a short line segment. The variance value evaluated along the direction θ_m on brightness becomes the minimum for those evaluated along all of the directions. Thus, by finding the minimum variance value, the filter detects the direction θ_m of the particle trajectory. The variance value is evaluated in a circular local domain; the parameter L refers to its radius.

shows the spatio-temporal $y-t$ sectional image having a moving particle at the direction θ_m in a spatio-temporal circular domain. When we evaluate the variance $s_I(\theta)$ on brightness along the direction θ, we obtain the minimum value of s_I at the direction θ_m,

$$s_I(\theta) = \frac{1}{2L+1} \sum_{l=-L}^{L} \{I(l,\theta) - \bar{I}\}^2 \quad \text{for} \quad 0 \leq \theta < \pi, \tag{20}$$

where L refers to the discrete radius of the circular domain, $I(l,\theta)$ refers to the spatio-temporal image brightness function having the polar coordinate system, and $\bar{I}$ does to the averaged brightness level along the direction θ,

$$\bar{I} = \frac{1}{2L+1} \sum_{l=-L}^{L} I(l,\theta). \tag{21}$$

Thus, we can determine the direction θ_m by finding the minimum variance of $s_I(\theta)$. Since the flow velocity is oscillating along the time coordinate system t, the direction $\theta_m(t)$ is also oscillating. (Note that the direction of a short line segment refers to a one-dimensional velocity component.) Analysing the temporal change of the direction $\theta_m(t)$ by the one-dimensional Fourier analysis method, we can determine the oscillation period T and the number of multiple periods K. In realistic situations that have many moving particles in fluid, many short line segments that represent the trajectories of the many particles exist on a spatio-temporal sectional image. When the velocity component u is not zero, the trajectory due to a particular particle is not clearly observed. However, a set of the many trajectories due to the many particles provides the oscillation period of temporally oscillating signals.

4. Experimental Results

4.1 Generating synthetic image sequences

We assumed the brightness distribution of a particle locating at a pixel site (x_0, y_0) to be the following function $B(x, y)$ (Raffel, 1998),

$$B(x,y) = B_0 \exp\left(-\frac{(x-x_0)^2 + (y-y_0)^2}{R^2/8}\right) \tag{22}$$

where B_0 refers to the maximum brightness level of the particle and R refers to its diameter. In the present experiments, the parameter B_0 was randomly distributed from 150 to 255 in 256 brightness levels; the background brightness level was fixed at 20.

We generated temporally oscillating flow fields at the fundamental oscillation period $T = 25.6$ (frames). The flow fields have translational, rotational and shear components as described by the following equations,

$$\begin{aligned} u(x,y,t) &= U_0 + U(t) - \omega(t)(y-y_c) + \sigma(t)(x-x_c), \\ v(x,y,t) &= V_0 + V(t) + \omega(t)(x-x_c) - \sigma(t)(y-y_c), \end{aligned} \tag{23}$$

where,

$$\begin{aligned} U(t) &= U_1 \sum_{h=1}^{H} \frac{1}{h} \cos\left(\frac{2\pi h t}{T} + \phi_{u_h}\right), \quad V(t) = V_1 \sum_{h=1}^{H} \frac{1}{h} \cos\left(\frac{2\pi h t}{T} + \phi_{v_h}\right), \\ \omega(t) &= \frac{P}{S_x} \sum_{h=1}^{H} \frac{1}{h} \cos\left(\frac{2\pi h t}{T} + \phi_{\omega_h}\right), \quad \sigma(t) = \frac{P}{S_x} \sum_{h=1}^{H} \frac{1}{h} \cos\left(\frac{2\pi h t}{T} + \phi_{\sigma_h}\right). \end{aligned} \tag{24}$$

The parameter H refers to the number of harmonics contained in a particular oscillation; the parameter varied as $H = 0, 1, 2, 3$. Each amplitude coefficient of the harmonics decreases with $1/h$. The parameters $\phi_{u_h}, \phi_{v_h}, \phi_{\omega_h}, \phi_{\sigma_h}$ refer to the phase shifts of the hth harmonics. The parameters U_0 and V_0 refer to the horizontal and vertical direct components of the oscillating velocity vector field; they were fixed at $(U_0, V_0) = (0.1, -0.2)$ (pixels/frame). The parameters (U_1, V_1) refer to the amplitude coefficients of the first harmonics in the translational component; they were fixed at $(U_1, V_1) = (0.3, -0.5)$ (pixels/frame) except the assessment of dynamic ranges. The set of the parameters (S_x, S_y) refers to the spatial size of an image plane; all of the synthetic image sequences have $S_x = S_y = 256$ (pixels). In generating flow fields, we partitioned an image plane into rectangular domains, the number of which is P^2. The particular domains have the spatial size of $(S_x/P) \times (S_y/P)$ (pixels^2). Equations (23) and (24) describe a flow field in a particular domain; a pixel site denoted by (x_c, y_c) refers to the centre position of the particular domain. Several different values of the discrete parameter $P = 1, 2, 3, 4, 5$ generate flow fields with different velocity gradients. The parameter P controls the maximum velocity gradient within a particular domain. As the parameter P increases, the velocity gradient also increases. Figure 2 shows a typical velocity vector field generated by Eqs. (23) and (24), and the temporal changes of two velocity components observed at a pixel site.

Image sequences utilised in the present experiments have the flow fields generated above; particles having the brightness function of Eq. (22) visualise the flow fields. To confirm the error dependence of the proposed methods on the density of particles d_p, we changed the diameter of Eq. (22) as $R = 2, 4, 6, 8, 10$ (pixels), and the number of particles as $N_p = 100, 200,$

Method	Model equations	Parameter values	
		For synthetic image	For real image
LOM+PA	Eq. (6) + Eq. (8) + Phase averaging	$L_x = L_y = 3$ (pixels) $L_t = 1$ (frame) $L_a = 0$ (pixel)	$L_x = L_y = 5$ (pixels) $L_t = 5$ (frames) $L_a = 2$ (pixels)
PM1	Eq. (6) + Eq. (8) + Eq. (13)	$L_x = L_y = 3$ (pixels) $L_t = 1$ (frame) $L_a = 0$ (pixel)	$L_x = L_y = 5$ (pixels) $L_t = 5$ (frames) $L_a = 2$ (pixels)
PM2	Eq. (6) + Eq. (15) + Eq. (16)	$L_x = L_y = 3$ (pixels) $M = 3$, $L_a = 0$ (pixel) $\beta = 1.0 \times 10^{-6}$	$L_x = L_y = 5$ (pixels) $M = 5$, $L_a = 2$ (pixels) $\beta = 1.0 \times 10^{-3}$
ACM	Eq. (1)+Eq. (2)	$L_x = L_y = 3$ (pixels) $L_t = 1$ (frame) $W_x = W_y = 2$ (pixels)	$L_x = L_y = 5$ (pixels) $L_t = 5$ (frames) $W_x = W_y = 2$ (pixels)

Table 1. Parameter values of the gradient-based methods (LOM+PA, PM1 and PM2) and the matching-based one (ACM) applied to synthetic and real image sequences. When the parameter values are not explicitly stated in the particular figures showing experimental results, the parameter values stated in this table were utilised. In LOM+PA, the phase-averaging processing was applied to velocity vectors having $|\vec{v}| < 2.0$ (pixels/frame) as post-processing except Fig. 6. Refer to Eqs. (11) and (12) for the estimation of spatio-temporal gradients on an image brightness distribution function required in the gradient-based methods. The frame number utilised for the analysis of the synthetic image sequences was $S_t = 128$ (frames) except Figs. 5(b) and 5(c).

300, 400, 500, 1000, 2000, 3000, 4000, 5000. Figure 3 shows snapshots of the synthetic image sequences. The density of particles d_p refers to the ratio of the number of the pixel sites having brightness levels higher than the background level to the number of the whole pixel sites.

4.2 Accuracy assessment

To confirm the performance of the two proposed methods, we applied the proposed methods and two ordinary ones to the synthetic image sequences generated above. We call the proposed method utilising the phase constancy assumption of Eq. (13) and the error function of Eq. (14) "PM1", and the other proposed method utilising the Fourier series of Eqs. (15) and (16) and the error function of Eq. (17) "PM2". We realised the local optimisation method as the ordinary gradient-based method. The method utilises the spatio-temporal local constancy assumption of Eq. (8) and the error function of Eq. (9). In addition, the method utilises a phase-averaging processing as post-processing. We call this ordinary gradient-based method "LOM+PA". We also realised the average correlation method "ACM" proposed by Meinhart et al. (2000) as the ordinary matching-based method. The method evaluates a reliable cross-correlation function by averaging cross-correlation functions obtained within a temporal local domain and/or at the time intervals of an oscillation period, as described in Section 2.1. These four methods LOM+PA, PM1, PM2 and ACM have several parameters. Table 1 shows the parameter values chosen for the four methods in the most of the following experiments.

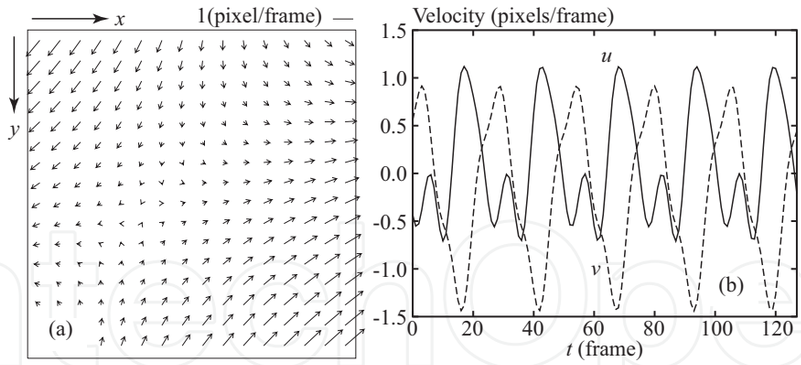

Fig. 2. Typical synthetic flow field and its temporal velocity change. (a) A flow filed at $t = 0$ (frame). (b) The temporal changes of the velocity components (u, v) observed at $(x, y) = (32, 32)$ (pixel). The spatial size of the flow field is $S_x \times S_y = 256 \times 256$ (pixels^2). The flow field was generated by Eqs. (23) and (24) with $(U_0 = 0.1, V_0 = -0.2)$ (pixels/frame), $(U_1 = 0.3, V_1 = -0.5)$ (pixels/frame) and $P = 1$. The number of harmonics was $H = 3$, the fundamental oscillation period was $T = 25.6$ (frames), and the phase shifts ϕ_{u_h}, ϕ_{v_h}, ϕ_{ω_h}, ϕ_{σ_h} of the hth harmonics were generated with random numbers.

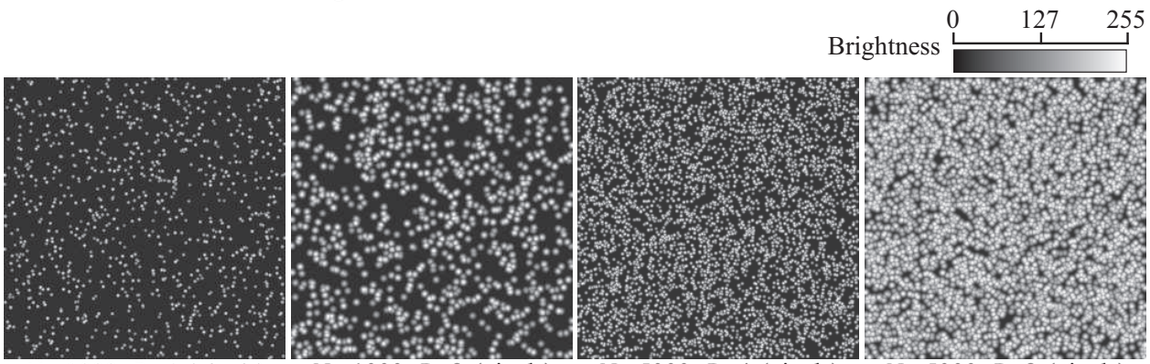

N_p=1000, R=4 (pixels) d_p=19.5 (%)
N_p=1000, R=8 (pixels) d_p=57.5 (%)
N_p=5000, R=4 (pixels) d_p=65.0 (%)
N_p=5000, R=8 (pixels) d_p=97.3 (%)

Fig. 3. Snapshots of synthetic image sequences. All of the sequences consist of the spatial size $S_x \times S_y = 256 \times 256$ (pixels^2). Image brightness was quantised into 256 levels. Refer to Eq. (22) for the brightness distribution function of a particle; B_0 was set to a random number in the range of $150 \leq B_0 \leq 255$. Particular images have $N_p = 1000, 5000$ particles with the diameter of $R = 4, 8$ (pixels). The parameter d_p (%) refers to the density of particles, which is the ratio of the number of the pixel sites having brightness levels higher than the background brightness level $B = 20$ to the spatial size $S_x \times S_y$.

The next root-mean-square (RMS) error measure E_r evaluates the accuracy of an obtained time-varying velocity vector field,

$$E_r = \sqrt{\frac{1}{N} \sum_{i=1}^{N} \left| \vec{v}_{d_i} - \vec{v}_{t_i} \right|^2} \tag{25}$$

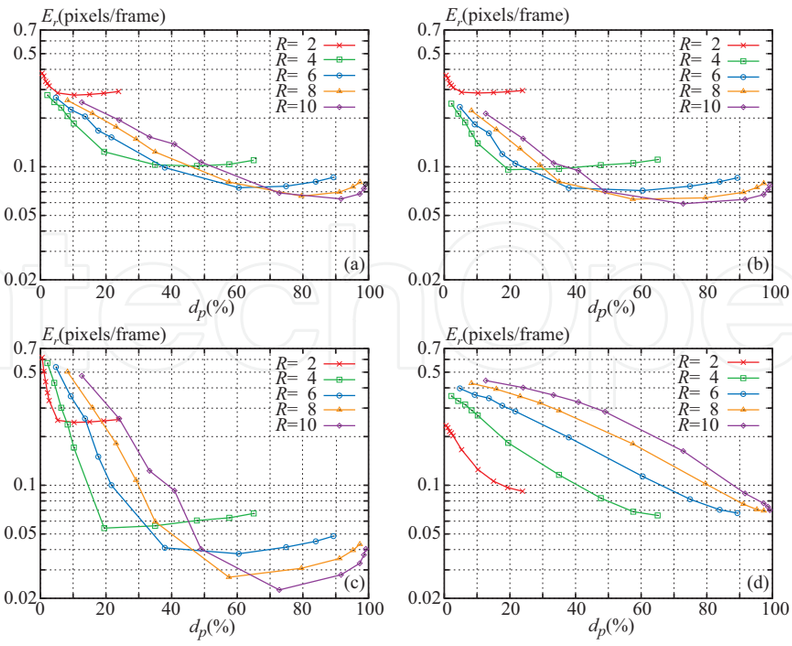

Fig. 4. Dependence of the RMS error measures E_r on the density of particles d_p. Image sequences were analysed by (a) LOM+PA, (b) PM1, (c) PM2 and (d) ACM; the sequences have the oscillating flow field with $H = 3$ and $P = 1$ (Fig. 2) and N_p = 100, 200, 300, 400, 500, 1000, 2000, 3000, 4000, 5000 particles with the diameter of $R = 2, 4, 6, 8, 10$ (pixels) (Fig. 3). Refer to Table 1 for the parameter values of the four methods and Eq. (25) for the RMS error measure.

where N refers to the number of all obtained velocity vectors, $\vec{v}_{d_i}(x, y, t) = (u_{d_i}, v_{d_i})$ refers to the ith obtained velocity vector (components) determined at the pixel site (x, y, t) and $\vec{v}_{t_i}(x, y, t) = (u_{t_i}, v_{t_i})$ refers to its corresponding true vector. Since ACM restricts the search area to ± 2 (pixels) with $W_x = W_y = 2$ (pixels) in computing a cross-correlation function (see Table 1), we discarded the velocity vectors having the absolute speed larger than 2.0 (pixels/frame) in computing the RMS error measure except the assessment of dynamic ranges.

First, we assessed the dependence of the RMS error measures on the density of particles d_p for the image sequences having the different diameters of R and the different numbers of particles N_p. Figure 4 shows the obtained dependence. As the density of particles d_p increases in its rather smaller range, the RMS error measures decrease for the gradient-based methods LOM+PA, PM1 and PM2. However, when d_p becomes large, the error measures again increase as d_p increases. In particular, the dependence obtained for PM2 show this trend of increasing error measures in the range of about $d_p > 70$ (%) for $R = 8, 10$ (pixels). The high density due to a large particle diameter and the large number of particles causes occluding boundaries among several particles. Along the occluding boundaries, it is difficult to estimate accurate gradients on a brightness pattern. In the gradient-based methods, erroneous gradients caused by the occluding boundaries bring erroneous velocity vectors. After the density of particles reaches at a saturated value such as $d_p = 90$ (%) with $R = 10$ (pixels), the occluding boundaries occupies most of an image sequence. Thus, the error measures highly increase as d_p increases under the saturated density. The dependence obtained for ACM differs from that for the gradient-based methods. The RMS error measures for ACM monotonically decrease as

the density of particles increases. The matching-based approach does not utilise gradients, but does a cross-correlation function between two successive image frames. The spatial arrangement of particles is important for computing a high reliable correlation function. When the density of particles is low, there are many candidates of pattern correspondences between two image frames. Thus, the correlation function obtained under such the low density has uncertainty in finding the peak position of the function. The high density of randomly distributed particles reduces the uncertainty in finding the peak position. The dependence obtained here shows that PM2 has the best accuracy among the four methods. In particular, the large size of the diameter such as $R = 8, 10$ (pixels) brings the best accuracy in the middle range of the density such as about $60 < d_p < 80$ (%). In addition, by comparing LOM+PA and PM1, we can recognise that PM1 is somewhat superior to LOM+PA in the low density of particles.
Figure 5(a) shows the dependence of the RMS error measures on the parameter P, which controls spatial velocity gradients. The four methods assume that a brightness pattern remains during its motion and that a flow field is locally uniform. As the parameter P increases, these assumptions on a rigid pattern and a uniform flow field become to be unmatched to the image sequences. The dependence obtained by the four methods shows similar trends that the RMS error measures become large as the parameter P increases.
The four methods assume that the oscillation period T is constant during the number of multiple periods K, namely, during $S_t = KT$. The ideal situation for the methods is that the oscillation period is constant during a huge number of image frames, and that all of these image frames are provided to determine velocity vector fields by the methods. In practical situations, we can utilise only a limited number of image frames. Figures 5(b) and 5(c) show the dependence of the RMS error measures on the frame number $S_t = KT$ for the image sequences having the number of particles $N_p = 1000$ and $N_p = 5000$. When the number of particles contained in an image sequence is small, such as, $N_p = 1000$, the error measures on the four methods decrease as the frame number S_t increases. When the number of particles is large, such as, $N_p = 5000$, the error measures on the methods except ACM do not decrease as the frame number increases. For the large number of particles, we can observe spatio-temporal brightness changes all over the image plane and during whole image frames. Therefore, the small number of image frames is enough for high accurate velocity determination. This result shows that increasing the frame number is effective when an image sequence has the small number of particles. When an image sequence has the large number of particles, increasing the frame number is not so effective for the accuracy improvement of the gradient-based approach. Furthermore, we compare the two gradient-based methods PM1 and PM2. When S_t is less than 64 (frames) in the result obtained for $N_p = 1000$ [Fig. 5(b)], PM1 is superior to PM2. The model utilised in PM2 has more unknown parameters, such as a_m, b_m, c_m, d_m than that in PM1. In order to estimate accurately many unknown parameters, it is necessary to have a huge number of data points. Thus, when S_t is small, there are not enough image frames, that is, not enough data points to achieve the accurate determination of the unknown parameters in PM2. When we determine an oscillating flow field with the slightly varying oscillation period and when the number of particles is small, we are not able to utilise many image frames. In this case, we can utilise PM1 to achieve better accuracy.
When the oscillation period T is enough large, or when a velocity vector field is stationary, we can expect more accuracy of the methods LOM+PA, PM1 and ACM by increasing the size L_t on the temporal constancy assumption. We confirmed the dependence of the RMS error measures on the parameter L_t for the several image sequences generated with the different values of $H = 0, 1, 2, 3$. Figures 5(d) and 5(e) show the obtained dependence. The parameter

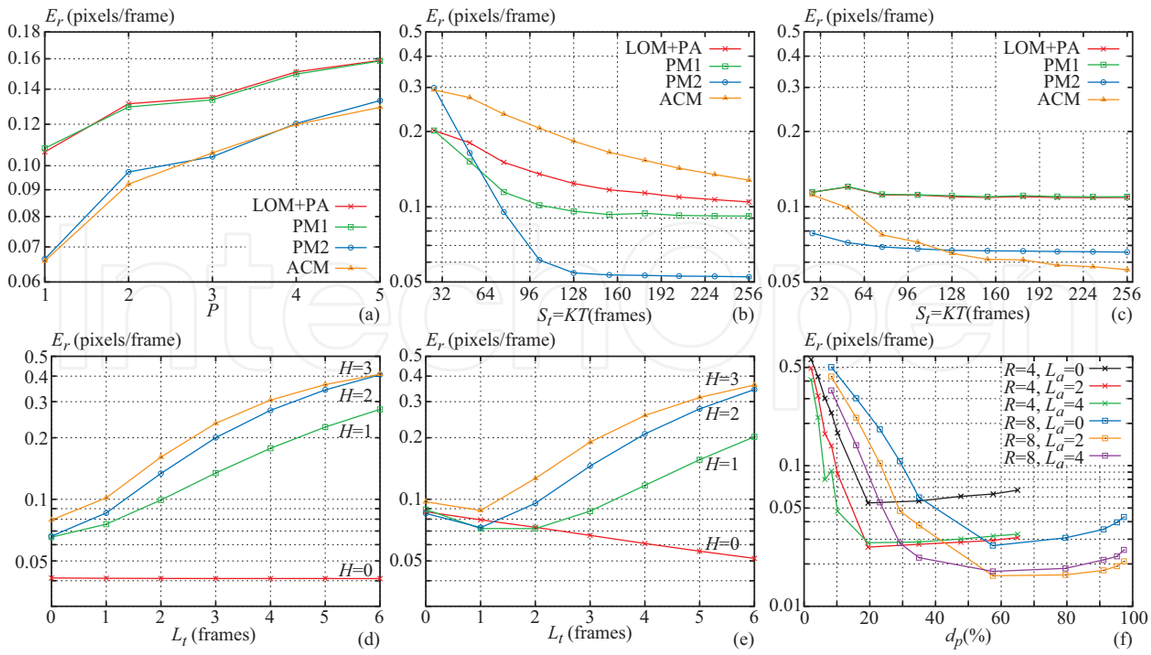

Fig. 5. Dependence of the RMS error measures E_r on several parameter values. Figure (a) shows the dependence on the parameter P of velocity gradients. The dependence was evaluated for LOM+PA, PM1, PM2 and ACM with the image sequences of $H = 3$ and $N_p = 5000$. Figures (b) and (c) shows the dependence on the frame number $S_t = KT$ (frames). The dependence was evaluated for LOM+PA, PM1, PM2 and ACM with the image sequences of $H = 3$, $P = 1$, and (b) $N_p = 1000$ and (c) $N_p = 5000$. Figures (d) and (e) shows the dependence on the parameter of the temporal local domain L_t. The dependence was evaluated for (d) PM1 and (e) ACM with the image sequences of $H = 0, 1, 2, 3$, $P = 1$, and $N_p = 3000$. Figure (f) shows the dependence on the density of particles d_p for the spatial size $L_a = 0, 2, 4$ (pixels) and the particle diameter $R = 4, 8$ (pixels). The dependence was evaluated for PM2 with the image sequences of $H = 3$, $P = 1$ and N_p = 100, 200, 300, 400, 500, 1000, 2000, 3000, 4000, 5000. We fixed a particle diameter of the image sequences utilised for the evaluation at $R = 4$ (pixels) except for (f). Refer to Table 1 for the parameter values of the four methods, Fig. 2 and Eqs. (23) and (24) for synthetic flow fields, Fig. 3 for synthetic images, and Eq. (25) for the RMS error measure.

H refers to the number of harmonics contained in the temporal change of an oscillating flow field [see Eq. (24)]. Thus, increasing the parameter H brings the shorter oscillation period. A flow field with $H = 0$ is stationary; a flow field with $H \geq 1$ has the harmonics with the oscillation period T/H (frames). On the dependence of PM1, as the parameter L_t increases, the error measures also increase monotonically except the dependence of $H = 0$. The dependence of ACM has the minimum RMS error measures at $L_t = 1$ or 2 (frames) for $H = 1$ and at $L_t = 1$ (frame) for $H = 2, 3$. From the dependence, we can increase the size L_t of ACM more than that of PM1. In addition, on the dependence of $H = 0$, we can highly increase the accuracy of ACM by increasing the size L_t, as compared with PM1.

In the above experiments, the gradient-based methods LOM+PA, PM1 and PM2 estimated the spatio-temporal gradients f_x, f_y, f_t by the forward difference method, which utilised the spatio-temporal domain consisting of 2×2 (pixels^2) and 2 (frames) and averaged the four values of the forward differences [see Eq. (11)]. We confirmed the dependence of the RMS error measures on the spatial size of the rectangular domain $(2L_a + 1) \times (2L_a + 1)$ (pixels^2), which were utilised for averaging the gradients [see Eq. (12)]. Figure 5(f) shows the dependence of the RMS error measures on the parameter L_a. The obtained dependence shows that we can improve the accuracy of PM2 by increasing the spatial size L_a. In particular, we can highly improve the accuracy with $L_a = 2$ (pixels), compared to that with $L_a = 0$ (pixel).

4.3 Assessment of dynamic ranges

The dynamic ranges of the four methods were assessed for synthetic image sequences having oscillating flow fields. The flow fields were generated with the parameter values of $U_1 = 0.3 \times Q$ (pixels/frame) and $V_1 = -0.7 \times Q$ (pixels/frame) for $Q = 1, 2, \cdots, 10$ in Eqs. (23) and (24). As the parameter Q increases, the difference between the maximum absolute velocity and the minimum one contained in a generated flow field also increases. The other parameters of Eqs. (23) and (24) have the same values as those of Fig. 2. The synthetic image sequences have N_p=5000 particles with the diameter of $R = 10$ (pixels).
The next equation evaluates the dynamic range D of a method,

$$D = (v_{t_{\max}} - v_{t_{\min}})/E_r, \tag{26}$$

where $v_{t_{\max}} = \max_i |\vec{v}_{t_i}|$ and $v_{t_{\min}} = \min_i |\vec{v}_{t_i}|$ respectively refer to the maximum absolute flow velocity and the minimum one of all the true velocity vectors $\vec{v}_{t_i}$ for $i = 1, 2, \cdots, N$, and E_r refers to the RMS error measure of Eq. (25) evaluated for the determined velocity vectors of $|\vec{v}_d| < 10$ (pixels/frame).
Figure 6 shows the dependence of the dynamic ranges on the parameter Q for the four methods. The gradient-based methods LOM+PA, PM1 and PM2 show the similar trends that the dynamic ranges D rapidly decrease around $Q = 2, 3, 4$ as the parameter Q increases. The dynamic ranges of the gradient-based methods finally reach the very small constant value about $D \simeq 1.3$. Since the gradient-based methods have difficulty on determining a large velocity vector, the RMS error measures become quite large for the large values of Q. In comparison to the dependence of the gradient-based methods, the matching-based method ACM shows the different dependence that the dynamic range D increases in the range of about $Q < 4$ and it reaches the almost constant large value about $D = 50 \sim 60$ in the range of about $Q > 5$. In determining large velocity, the matching-based approach is essentially much more suitable than the gradient-based one.
By comparing the dynamic ranges of the four methods, we confirmed that the dynamic range of the matching-based method is larger than those of the gradient-based ones. However, when focusing on low flow speed ($Q = 1$), we confirmed that the dynamic ranges of the gradient-based methods are larger than the matching-based one. When we analyse a real image sequence without preliminary knowledge on a velocity vector field, the matching-based approach is better than the gradient-based one, since the maximum flow velocity is preliminary unknown in practical situations. However, when we furthermore require dense and accurate analysis for low flow speed, we can utilise the gradient-based approach having the larger dynamic range for the low flow speed. By combining the matching-based approach with the gradient-based one according to the proposal of Sugii et al. (2000), we can expect to realise the new method having the large dynamic range for the large range of flow speed.

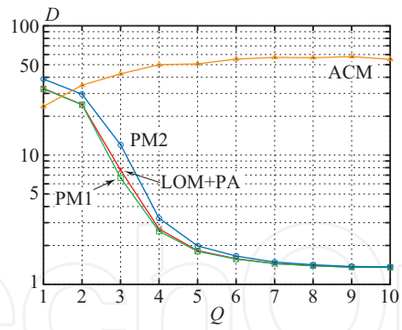

Fig. 6. Dependence of the dynamic range D [Eq. (26)] on the parameter Q. Image sequences utilised here have the oscillating flow fields generated with $H = 3$, $P = 1$, $(U_0 = 0.1, V_0 = -0.2)$ (pixels/frame), $T = 25.6$ (frames) and $(U_1 = 0.3 \times Q, V_1 = -0.7 \times Q)$ (pixels/frame) for $Q = 1, 2, 3, \cdots, 10$. The size of the image sequences is $S_x \times S_y = 256 \times 256$ (pixels^2) and $S_t = 128$ (frames). The image sequences have $N_p = 5000$ particles with the diameter of $R = 10$ (pixels). The four methods LOM+PA, PM1, PM2 and ACM were applied to the image sequences. The parameter values of the four methods were as follows: $L_x = L_y = 10$ (pixels), $L_t = 0$ (frame) for all of the methods, $L_a = 0$ (pixel) for the gradient-based methods LOM+PA, PM1 and PM2, $M = 3$ and $\beta = 1.0 \times 10^{-6}$ for PM2 and $W_x = W_y = 10$ (pixels) for ACM. Determined velocity vectors having $|\vec{v}_d| < 10$ (pixels/frame) were utilised for the evaluation of a dynamic range.

4.4 Stability of the proposed method PM2 on the number of harmonics

The method PM2 has the parameter M that refers to the number of harmonics contained in a temporal velocity change. The parameter M is unknown in practical situations. Figure 7(a) shows the dependence of the RMS error measures on the parameter M for three experimental conditions [Figs. 7(a-1), 7(a-2) and 7(a-3)], and two additional ones [Figs. 7(a-4) and 7(a-5)]. The image sequences analysed here have the oscillating flow field with $H = 3$. Thus, according to the value $H = 3$, the parameter M of PM2 should be larger than 3. The method PM2 also has the parameter β, which refers to the ratio between the maximum singular value and the threshold one for the singular value decomposition. The dependence of Figs. 7(a-1), 7(a-2) and 7(a-3) was obtained with $\beta = 1.0 \times 10^{-6}$; that of Figs. 7(a-4) and 7(a-5) was obtained with $\beta = 1.0 \times 10^{-3}$.

Figure 7(a-1) shows the dependence obtained for the experimental condition of $N_p = 5000$ and $L_x = L_y = 3$ (pixels). The dependence is almost flat in the range of $M \geq 3$. Figure 7(a-2) shows the dependence obtained for the experimental condition of $N_p = 1000$ and $L_x = L_y = 3$ (pixels). The dependence shows the similar trend to that of Fig. 7(a-1). However, the error measure slightly increases as the parameter M increases, in particular, in the range of $M \geq 12$. In comparison to the dependence of Figs. 7(a-1) and 7(a-2), the dependence of Fig. 7(a-3) obtained for the experimental condition of $N_p = 5000$ and $L_x = L_y = 0$ (pixel) shows that the error measure more rapidly increases as the parameter M increases in the range of $M > 3$. When the number of particles N_p is small, and/or when the spatial sizes of L_x and L_y are small, there is little brightness change utilised for velocity determination. Thus, the dependence of Figs. 7(a-1), 7(a-2) and 7(a-3) shows that the small number of particles and/or the small spatial sizes of L_x and L_y cause error in particular for the larger number of M. The proposed method PM2 with the parameter value of $\beta = 1.0 \times 10^{-3}$ provided the

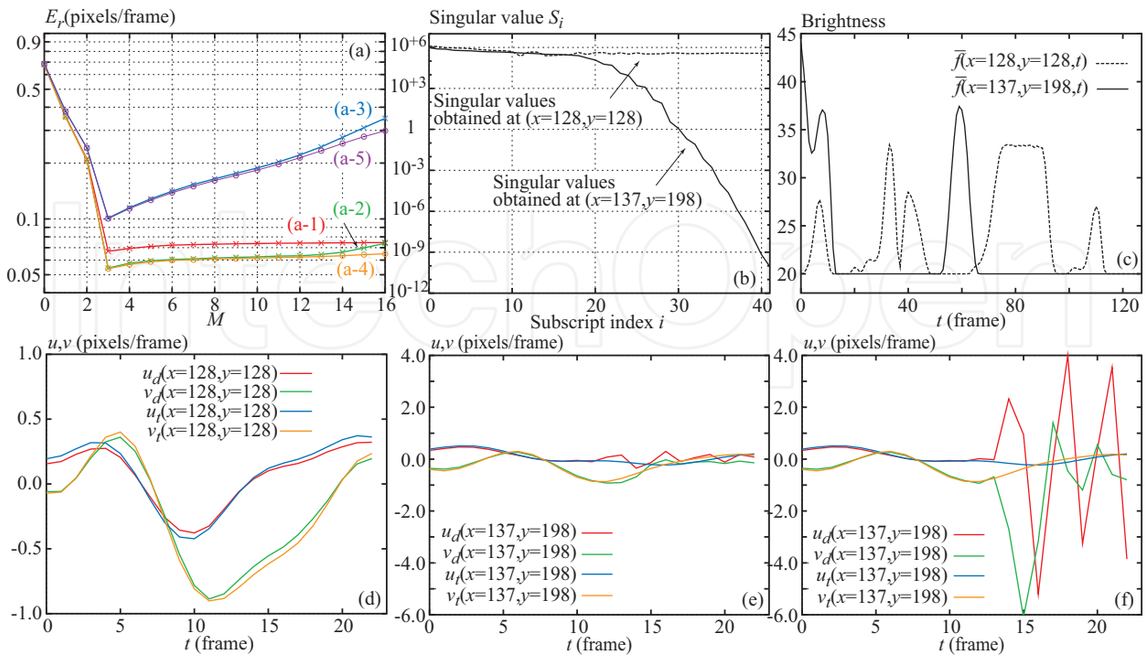

Fig. 7. Performance of the proposed method PM2 and its instability on the parameter M referring to the number of harmonics. (a) The dependence of the RMS error measures E_r on the parameter M. The image sequence analysed in (a-1), (a-3) and (a-5) has $N_p = 5000$ particles with the diameter of $R = 4$ (pixels); the sequence done in (a-2) and (a-4) has $N_p = 1000$ particles with the same diameter. The parameters L_x and L_y were $L_x = L_y = 3$ (pixels) in (a-1), (a-2) and (a-4) and $L_x = L_y = 0$ (pixel) in (a-3) and (a-5). The parameter β was $\beta = 1.0 \times 10^{-6}$ in (a-1), (a-2) and (a-3) and $\beta = 1.0 \times 10^{-3}$ in (a-4) and (a-5). (b) The two sets of singular values S_i obtained by the singular value decomposition. One of the two sets was obtained at the pixel site $(x = 128, y = 128)$ (pixel) and the other one was done at $(x = 137, y = 198)$ (pixel). The parameter values utilised here were $L_x = L_y = 0$ (pixel) and $M = 10$. The horizontal coordinate refers to the subscript index i in the range of $0 \leq i < (2 + 4M)$ and the vertical one does to the ith singular value S_i. (c) Temporal brightness changes observed at the two pixel sites $(x = 128, y = 128)$ (pixel) and $(x = 137, y = 198)$ (pixel). Brightness was averaged within the spatial local domain consisting of 7×7 (pixels^2) at a particular frame. (d) The temporal changes of two velocity components (u_d, v_d) determined at the pixel site $(x = 128, y = 128)$ (pixel) and those of their corresponding true ones (u_t, v_t). The parameter values utilised here were $L_x = L_y = 0$ (pixel), $M = 10$ and $\beta = 1.0 \times 10^{-6}$. (e) The temporal changes of two velocity components (u_d, v_d) determined at the pixel site $(x = 137, y = 198)$ (pixel) and those of their corresponding true ones (u_t, v_t). The parameter values utilised here were the same as (d) except $\beta = 1.0 \times 10^{-3}$. (f) The temporal changes of two velocity components (u_d, v_d) determined at the same pixel site as (e) and their corresponding true ones (u_t, v_t). The parameter values utilised here were the same as (d). The image sequence utilised in (b) $\sim$ (f) has $N_p = 1000$ particles with the diameter of $R = 4$ (pixels) (Fig. 3). All of the image sequences have the oscillating flow field with $H = 3$ and $P = 1$ (see Fig. 2). Refer to Table 1 for the other parameter values of PM2 and Eq. (25) for the RMS error measure.

better dependence as shown in Figs. 7(a-4) and 7(a-5) in the larger number of M. Note that the experimental conditions and the parameter values were the same between Figs. 7(a-2) and 7(a-4) and between Figs. 7(a-3) and 7(a-5), except the parameter value of β.

Let us focus on the difference between the dependence of Fig. 7(a-2) and that of Fig. 7(a-4). With the parameter value of $M = 10$, the RMS error measure with $\beta = 1.0 \times 10^{-3}$ in Fig. 7(a-4) is smaller than that with $\beta = 1.0 \times 10^{-6}$ in Fig. 7(a-2). Figures 7(b) $\sim$ 7(f) show numerical situations that caused error in the velocity determination with $\beta = 1.0 \times 10^{-6}$, and that avoided the error with $\beta = 1.0 \times 10^{-3}$. Figure 7(b) shows the two sets of singular values obtained by the singular value decomposition at the two pixel sites $(x = 128, y = 128)$ (pixel) and $(x = 137, y = 198)$ (pixel). Since the method PM2 solves the set of linear equations Eq. (18) by utilising the singular value decomposition, the method provides a set of singular values at a particular pixel site.

There is a large difference between the two sets of singular values. On the one hand, all of the singular values obtained at $(x = 128, y = 128)$ (pixel) are almost similar in their magnitude. The ratio $\min_i(S_i)/\max_i(S_i)$ between the minimum singular value and the maximum one is larger than 0.1. On the other hand, the ratio computed for the singular values obtained at $(x = 137, y = 198)$ is quite small [$\min_i(S_i)/\max_i(S_i) \simeq 10^{-16}$]. Singular values much smaller than the maximum one are numerically meaningless and harmful in solving the set of linear equations (Press et all., 1988). (This situation is so-called "ill-condition".) The value of $\beta \max_i(S_i)$ refers to the threshold value for the rejection of much smaller singular values. The appropriate parameter value of β for the singular value decomposition can suppress the error due to little brightness change and can avoid the instability of PM2.

Figure 7(c) shows clear difference between the temporal brightness changes observed at the two pixel sites $(x = 128, y = 128)$ (pixel) and $(x = 137, y = 198)$ (pixel), where brightness was averaged within the spatial local domain consisting of 7×7 (pixels^2) at a particular frame. The temporal brightness change observed at $(x = 137, y = 198)$ (pixel) has little brightness change, compared to that observed at the pixel site $(x = 128, y = 128)$ (pixel). The brightness change is insufficient for velocity determination at the pixel site $(x = 137, y = 198)$. This is the reason why some of the singular values obtained at the pixel site $(x = 137, y = 198)$ (pixel) are very small compared to other singular values.

At the pixel site $(x = 128, y = 128)$ (pixel) having much brightness change, PM2 determined an accurate velocity vector with either $\beta = 1.0 \times 10^{-3}$ or $\beta = 1.0 \times 10^{-6}$. Figure 7(d) shows the temporal changes of the two velocity components u_d and v_d obtained at the pixel site and their corresponding true ones u_t and v_t. The obtained velocity components are quite similar to the true ones. The two velocity components u_d and v_d were obtained with $\beta = 1.0 \times 10^{-6}$. Therefore, we can restate that the much brightness change does not cause the instability of PM2. In this case, we do not have to mention the choice of the parameter value β.

At the pixel site $(x = 137, y = 198)$ (pixel) having little brightness change, the temporal changes of the two velocity components u_d and v_d obtained with $\beta = 1.0 \times 10^{-3}$ [see Fig. 7(e)] differ from those obtained with $\beta = 1.0 \times 10^{-6}$ [see Fig. 7(f)]. The temporal changes of Fig. 7(e) are much better than those of Fig. 7(f). The comparison between the two figures of Figs. 7(e) and 7(f) shows that the singular value decomposition with the appropriate parameter β suppresses error in the determination of a velocity vector field and avoids the instability of PM2. However, the method automatically choosing an appropriate parameter β is still the problem.

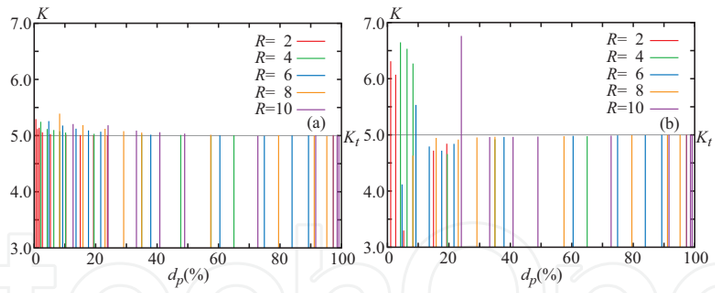

Fig. 8. Performance of the two proposed methods determining the number of multiple periods. The horizontal coordinates refer to the density of particles d_p and the vertical ones do to the determined number of multiple periods K. The height of a particular impulse shows the determined number K. The true number is $K_t = 5.0$. Both the figures omitted impulses being out of the range $3.0 \leq K \leq 7.0$. Figure (a) was obtained by the proposed method analysing the temporal changes of velocity vectors by the Fourier analysis method; the velocity vectors were tentatively determined by the ordinary gradient-based method of Eq. (7). Figure (b) was obtained by the proposed method analysing spatio-temporal sectional images by also the Fourier analysis method. Both the figures were obtained from the synthetic image sequences having the oscillating flow field with $H = 3$ and $P = 1$ (Fig. 2) and N_p = 100, 200, 300, 400, 500, 1000, 2000, 3000, 4000, 5000 particles with the diameter of $R = 2, 4, 6, 8, 10$ (pixels) (Fig. 3).

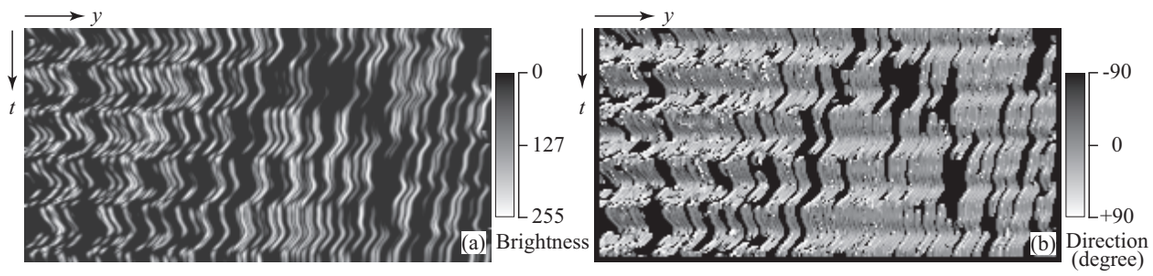

Fig. 9. Spatio-temporal sectional image and its direction distribution map utilised in the determination of an oscillation period and the number of multiple periods. The spatio-temporal sectional image (a) was sliced from a synthetic image sequence at $x = 64$ (pixel) within the $y - t$ plane. The sequence has the oscillating flow field with $H = 3$ and $P = 1$ (Fig. 2) and $N_p = 5000$ particles with the diameter of $R = 4$ (pixels). The size of the sequence is $S_x \times S_y = 256 \times 256$ (pixels^2) and $S_t = 128$ (frames). The direction distribution map (b) was obtained from the image (a) by the spatio-temporal filter detecting the direction of a short line segment. The parameter L of the filter in Eq. (20) was set to 3 (pixels) [see also Fig. 1(b)].

4.5 Performance of the methods determining the number of multiple periods

We investigated the performance of the two methods determining the number of multiple periods K from an image sequence. As described in the section 3.2, one of the two methods analyses tentatively determined velocity vectors by the Fourier analysis method; the other one analyses the temporal changes of pattern directions on spatio-temporal sectional images by also the Fourier analysis method.

Figure 8 shows the number of multiple periods K determined by the two methods from synthetic image sequences. The number K determined by the former proposed method analysing

tentatively determined velocity vectors is almost correct for most of the synthetic image sequences. The latter proposed method analysing spatio-temporal sectional images provided several erroneous results under the condition of about $d_p < 30$ (%). Under the low density of d_p, the latter method provided several abnormal results having huge error, compared to the former method.
Figure 9 shows a spatio-temporal sectional image sliced from a synthetic image sequence and its direction distribution map obtained by the direction detection filter. Since the latter proposed method analyses brightness patterns on a spatio-temporal sectional image, its performance directly depends on the density of particles. Furthermore, the latter proposed method assumes that particles are oscillating on a spatio-temporal sectional image of a $y - t$ image plane or a $x - t$ image plane (Fig. 1). However, the assumption is not satisfactory for the synthetic image sequence.
By comparing the results obtained by the two methods, we can conclude that the former proposed method is better than the latter one in particular under the low density of particles. Under the high density of particles, such as $d_p > 50$ (%), both the methods work well.

4.6 Analysis of a real image sequence

We present the experimental results obtained when applying the methods LOM+PA, PM1, PM2 and ACM to a real image sequence. The sequence was captured through a camera for the Karman vortices flow field visualised by particles with the sampling frequency of 30 (Hz) [Fig. 10(a)]. We obtained a frequency distribution on brightness from the real image sequence as shown in Fig. 10(b). We estimated the threshold level segmenting the particle region, which has higher brightness levels, from the background region. The estimated threshold level was 100 in 256 brightness levels. By counting the number of pixel sites which had brightness levels larger than the threshold one, we estimated the density of particles to be $d_p = 47.3$ (%).
To confirm the maximum flow speed contained in the real image sequence, we determined a time-varying velocity vector field by an ordinary matching-based method. While the matching-based approach is appropriate for a high flow speed, the gradient-based approach is not appropriate for a high flow speed of more than 1.0 (pixel/frame). We applied the ordinary matching-based method to a real image sequence re-sampled from the original real image sequence. The sampling frequency of the re-sampled image sequence was 15 (Hz). The ordinary matching-based method has the template consisting of the 7×7 (pixels^2) rectangular domain [$L_x = L_y = 3$ (pixels)]; the search area is the 11×11 (pixels^2) rectangular domain [$W_x = W_y = 5$ (pixels)]. Figure 10(c) shows a frequency distribution on determined absolute speed. The distribution shows that most of the pixel sites (98 %) have an absolute speed of less than 2.0 (pixels/frame), which corresponds to 1.0 (pixel/frame) in the original real image sequence. Thus, most of the velocity vectors are appropriate for the gradient-based approach. This result allowed us to apply the gradient-based methods to the original real image sequence.
We determined the number of multiple periods K and the oscillation period T from the real image sequence. First, we determined the parameters K and T by the proposed method analysing the temporal change of a tentatively determined velocity vector field. Figure 11(a) shows the temporal changes of the two velocity components tentatively determined by the ordinary gradient-based method with the local optimisation. The application of the Fourier analysis method to the temporal velocity changes provided power spectrum distribution functions. Figure 11(b) shows the sum of the functions obtained at all of the pixel sites for both the velocity components. The maximum peak position in the averaged power spectrum dis-

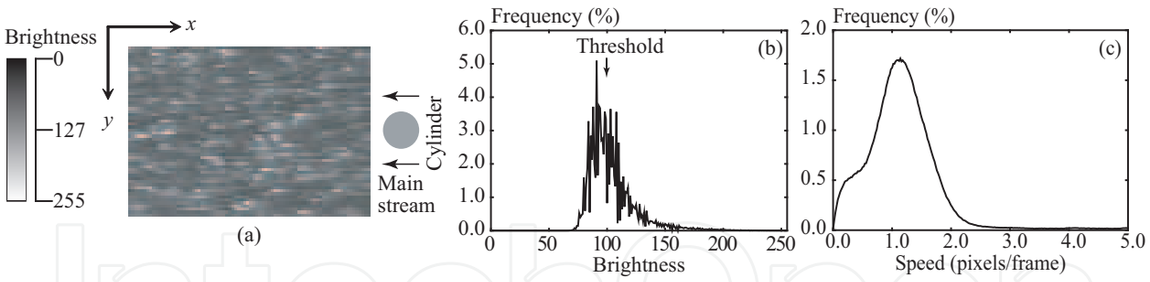

Fig. 10. Real image sequence of the Karman vortices flow field visualised by particles. (a) A snapshot of the image sequence. The size of the sequence is $S_x \times S_y = 80 \times 56$ (pixels^2) and $S_t = 1856$ (frames). Image brightness was quantised into 256 levels. The sampling frequency was 30 (Hz). The main stream was directed from right to left. A cylinder was located at the right side. (b) Frequency distribution on brightness. The threshold brightness level segmenting the foreground expressing particles from the background was estimated to be 100 in 256 brightness levels. The density of particles was estimated as $d_p = 47.3$ (%). (c) Frequency distribution on absolute speed determined by an ordinary matching-based method with a sub-pixel approximation method. The matching-based method was applied to an image sequence re-sampled from the original real image sequence (a) with the sampling frequency of 15 (Hz).

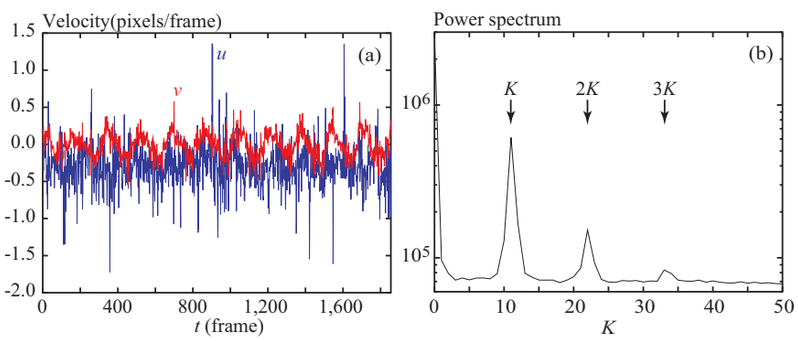

Fig. 11. Determination of the number of multiple periods K from the real image sequence of Fig. 10. (a) The temporal changes of the two velocity components u and v determined at the centre of the image plane by the local optimisation method. The spatio-temporal local domain $\delta S \times \delta T$ for the constancy assumption consists of 3×3 (pixels^2) and 3 (frames) [$L_x = L_y = 1$ (pixel) and $L_t = 1$ (frame)]. (b) Power spectrum distribution function obtained by the one-dimensional temporal Fourier analysis method from the temporal changes of both the velocity components. The maximum peak position in the distribution function provides the number of multiple periods $K = 11.019$ and the oscillation period $T = 168.4$ (frames).

tribution function provided $K = 11.019$ and $T = 168.4$ (frames). Next, we applied the other proposed method analysing spatio-temporal sectional images to the real image sequence. Figure 12(a) shows a spatio-temporal sectional image on the $y - t$ plane sliced at the centre pixel site of the image plane. The filter detecting the direction of a short line segment provides the direction distribution map of Fig. 12(b). The application of the temporal Fourier analysis method to the direction distribution maps obtained at all of the pixel sites provided power spectrum distribution functions. Figure 12(c) shows the sum of the power spectrum distri-

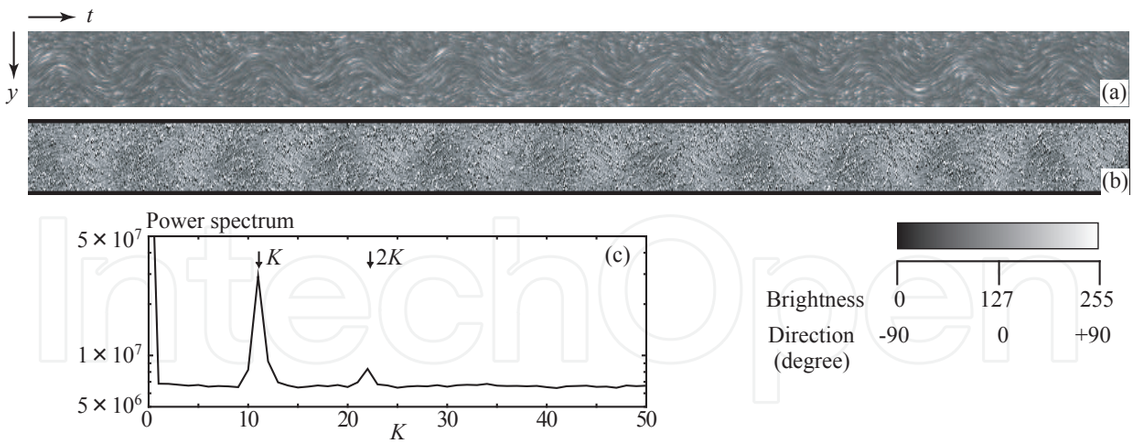

Fig. 12. Determination of the number of multiple periods K from the real image sequence of Fig. 10. (a) Spatio-temporal sectional image sliced at the centre of the image plane within the $y - t$ plane. (b) Direction distribution map obtained by the spatio-temporal filter detecting the direction of a short line segment from the spatio-temporal sectional image. The parameter L referring to the size of the circular local domain of the filter was set to 3 (pixels) [Fig. 1(b)]. (c) Power spectrum distribution function obtained by the one-dimensional temporal Fourier analysis method from the direction distribution map. The maximum peak position provides $K = 11.012$ and the oscillation period $T = 168.5$ (frames).

bution functions. The maximum peak position of the function provided $K = 11.012$ and $T = 168.5$ (frames). Since we can clearly distinguish the peak positions in both the power spectrum distribution functions Figs. 11(b) and 12(c), we can expect that both the determined oscillation periods are reliable. However, the previous results obtained for the synthetic image sequences (see Section 4.5) show that the former method analysing tentatively determined velocity vectors works better than the other latter one. Thus, we utilise $K = 11.019$ and $T = 168.4$ (frames) in the following analysis. In addition, the power spectrum distribution function [Fig. 11(b)] obtained by the former method shows that there exists at least the third harmonics in the temporal change of the flow field. This result implies that the parameter M for PM2 should be larger than 3.

We determined velocity vector fields from the real image sequence by LOM+PA, PM1, PM2 and ACM with the above parameters $K = 11.019$ and $T = 168.4$ (frames). Table 1 shows the parameter values utilised in the four methods. Figure 13(a) shows the temporal changes of velocity vectors determined at the centre of the image plane. The horizontal components u determined by the four methods show very similar temporal changes. The vertical components v determined by the gradient-based methods LOM+PA, PM1 and PM2 are smaller than that of the matching-based method ACM in their amplitude. To confirm the validity of the vertical components, we roughly determined the vertical velocity component v around the centre of the image plane, by tracking a distinguishable particle with the naked eyes during $t = 86 \sim 128$ (frame). The result of the rough determination was about $v = -0.35 \sim -0.40$ (pixels/frame). Thus, by comparing this result with Fig. 13(a), we confirm that the result of ACM is more consistent with that of the naked eyes than those of the gradient-based methods on the vertical velocity component.

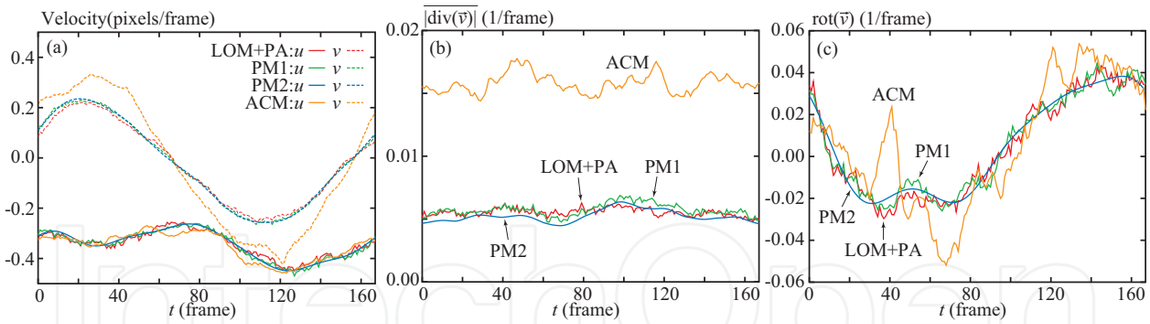

Fig. 13. Comparison among the velocity vector fields determined by LOM+PA, PM1, PM2 and ACM from the real image sequence of Fig. 10. (a) The temporal changes of the velocity components (u, v) determined at the centre of the image plane. (b) The temporal changes of the divergence measures $\overline{|\mathrm{div}(\vec{v})|}$ averaged over an image plane at a particular frame. (c) The temporal changes of the rotation values $\mathrm{rot}(\vec{v})$ obtained at the centre of the image plane. Refer to Table 1 for the parameter values of the four methods.

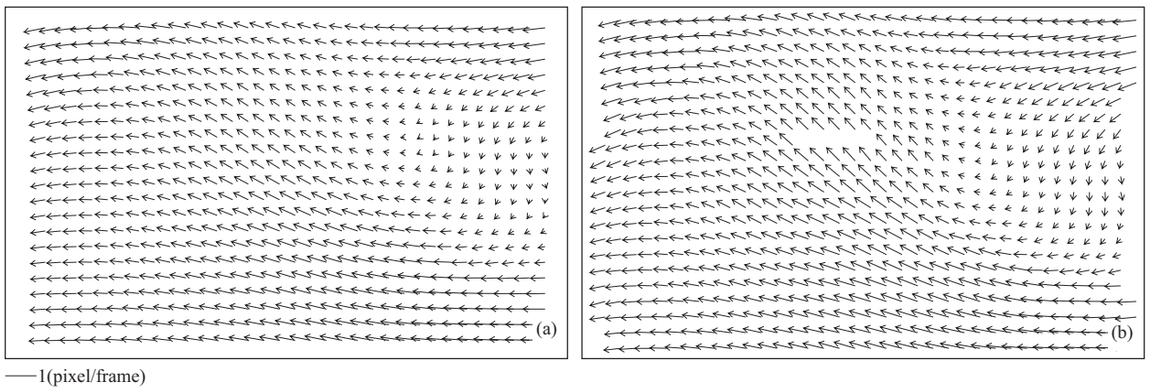

Fig. 14. Velocity vector fields determined by (a) PM2 and (b) ACM from the real image sequence of Fig. 10. Both the fields were obtained at $t = 120$ (frame). Refer to Table 1 for the parameter values of PM2 and ACM.

We measured the average of the absolute divergence $\overline{|\mathrm{div}(\vec{v})|}$ for each of the determined velocity vector fields at a particular frame. Since the divergence measure is expected to be zero for a non-compressible fluid flow field, it becomes a good measure to show accuracy on a determined velocity vector field. Figure 13(b) shows the temporal changes of the divergence measures; the measures of LOM+PA, PM1 and PM2 are much smaller than that of ACM.
Furthermore, we also measured the rotation value $\mathrm{rot}(\vec{v})$ for each of the determined velocity vector fields. Figure 13(c) shows the temporal changes of the rotation measures at the centre of the image plane. These temporal changes show similar signals. However, the temporal change of ACM has the several unusual values of $\mathrm{rot}(\vec{v})$ at about $t = 40, 70, 120$ (frame). Figures 14(a) and 14(b) respectively show the velocity vector fields determined by PM2 and ACM at $t = 120$ (frame). The velocity vector field determined by ACM lacks some vectors around its centre. (Such the regions lacking vectors suddenly appear and disappear.) We do not clearly understand the mechanism causing the unusual values of $\mathrm{rot}(\vec{v})$ and the lack of

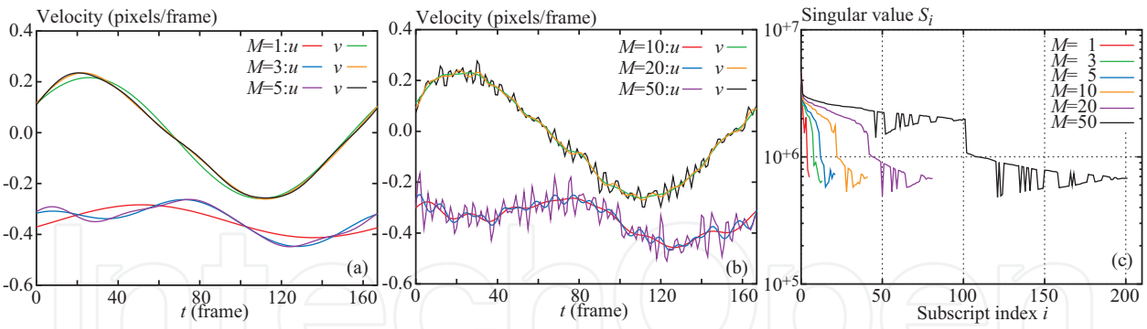

Fig. 15. Temporal changes of two velocity components (u, v) and the sets of singular values obtained by the proposed method PM2 from the real image sequence (Fig. 10). The temporal changes were obtained with the parameter values of (a) $M = 1, 3, 5$ and (b) $M = 10, 20, 50$. (c) The sets of the singular values S_i were obtained with $M = 1, 3, 5, 10, 20, 50$. All of the results were obtained at the centre of the image plane. The horizontal coordinate in (c) refers to the subscript index i in the range of $0 \leq i < (2 + 4M)$ and the vertical one does to the ith singular value S_i. Refer to Table 1 for the other parameter values of PM2.

velocity vectors. Figure 13(c) shows that the unusual values appear at the frames having high rotational values. In addition, Fig. 14(b) shows that the region lacking vectors exists around the high rotational field. Thus, the unusual changes and the regions lacking vectors seem to be caused by high rotational fields. We expect that the combination of ACM and the higher order matching-based approach (e.g. Scarano, 2002) solves this problem.

Finally, we analysed the real image sequence by PM2 with several different parameters of M. Figure 15 shows the temporal changes of velocity vectors obtained with $M = 1, 3, 5, 10, 20, 50$ at the centre of the image plane. The parameter value $M = 1$ is too small to express the temporal change of the velocity vector. In particular, the temporal change of the horizontal component u determined with $M = 1$ clearly differs from those with $M = 3, 5$ as shown in Fig. 15(a). The parameter value $M = 50$ is too large; we obtained the noisy components as shown in Fig. 15(b). Figure 15(c) shows the sets of singular values obtained by the singular value decomposition at the centre of the image plane. The ratio of the minimum singular value to the maximum one is about $1/10$ for all of the parameter values $M = 1, 3, 5, 10, 20, 50$. Since all of the singular values S_i were larger than the threshold value $\beta \max_i(S_i)$ for $\beta = 1.0 \times 10^{-3}$, all of them were utilised in solving the set of linear equations. The previous result for the synthetic image sequences (Fig. 7) shows that the singular value decomposition can avoid erroneous results due to the high harmonics with the appropriate parameter β. However, the real experimental result shows that the proposed method PM2 also requires further development on choosing the appropriate parameters M and β. The combination of the singular value decomposition and the methods automatically choosing the appropriate parameters M and β is expected to improve the accuracy and the stability of the proposed method PM2.

5. Conclusion

We proposed two methods for determining oscillating velocity vector fields in the gradient-based approach. One of the methods utilises a phase-constancy assumption on velocity; the other one does the Fourier series expressing a temporal velocity change. Both the proposed

methods take account of the oscillation characteristic in their error functions. The proposed two methods preliminarily require the parameters of an oscillation period and the number of multiple periods. Thus, we have also proposed two methods for determining the parameters in advance. One of the methods analyses the temporal changes of velocity vectors tentatively determined by an ordinary gradient-based method; the other method analyses spatio-temporal sectional images sliced from an original image sequence. Both the methods utilise the one-dimensional Fourier analysis method; the maximum peak position of an obtained power spectrum distribution provides the parameters.

The proposed gradient-based methods were compared to ordinary gradient- and matching-based methods through the analysis of synthetic and real image sequences. Results for the synthetic image sequences show that the proposed method utilising the Fourier series achieves the best accuracy for the image sequences having huge image frames, low flow speed and the middle density of particles. When the flow speed is high, the ordinary matching-based method is better. When the number of image frames utilised for analysis is small, the proposed method utilising the phase-constancy assumption as an additional constraint is better than the other proposed method. In addition, we confirmed performance of the proposed two methods determining an oscillation period and the number of multiple periods for the synthetic image sequences. Both the methods work well under the high density of particles. The method analysing tentatively determined velocity vectors works better than the other one analysing a spatio-temporal sectional images under the low density.

There are three future research topics. The first one is on the instability of the proposed method utilising the Fourier series. The method becomes unstable, when the number of harmonics becomes large. The singular value decomposition can partially avoid the instability by the choice of an appropriate threshold value utilised for the rejection of obtained small singular values. However, the proposed method still requires an additional method automatically choosing the appropriate threshold value as well as the appropriate number of harmonics. The second one is on a dynamic range. The gradient-based approach is generally inappropriate to high flow speed, in comparison to the matching-based method. Oscillating velocity vector generally ranges from low flow speed to high flow speed. Thus, a wide dynamic range is required for oscillating flow fields in PIV. The combination of the proposed gradient-based methods with the ordinary matching-based one is expected to achieve the wide dynamic range. The last one is on the constancy assumption of the oscillation period. Since the proposed methods assume the oscillation period to be constant, they are not applicable to image sequences with time-varying oscillation period. We need to solve the limitation of assuming the constant oscillation period for more realistic situations.

6. References

Adrian, R. J. (1991). Particle-imaging techniques for experimental fluid mechanics, *Annual Review of Fluid Mechanics* **Vol. 23**: 261–304.

Astarita, T. (2009). Adaptive space resolution for PIV, *Experiments in Fluids* **Vol. 46** (No. 6): 1115–1123.

Corpetti, T., Mémin, É. & Pérez, P. (2002). Dense estimation of fluid flows, *IEEE Transactions on Pattern Analysis and Machine Intelligence* **Vol. 24** (No. 3): 365–380.

Cowen, E. A. & Monismith, S. G. (1997). A hybrid digital particle tracking velocimetry technique, *Experiments in Fluids* **Vol. 22** (No. 3): 199–211.

Fincham, A. & Delerce, G. (2000). Advanced optimization of correlation imaging velocimetry algorithms, *Experiments in Fluids* **Vol. 29** (Supplement 1): S13–S22.

Hart, D. P. (2000). PIV error correction, *Experiments in Fluids* **Vol. 29** (No. 1): 13–22.
Hassan, Y. A., Blanchat, T. K. & Seeley, C. H. (1992). PIV flow visualisation using particle tracking techniques, *Measurement Science and Technology* **Vol. 3** (No. 7): 633–642.
Horn, B. K. P. & Schunck, B. G. (1981). Determining optical flow, *Artificial Intelligence* **Vol. 17** (No. 1–3): 185–203.
Kearney, J. K., Thompson, W. B. & Boley, D. L. (1987). Optical flow estimation: an error analysis of gradient-based methods with local optimization, *IEEE Transactions on Pattern Analysis and Machine Intelligence* **Vol. PAMI–9** (No. 2): 229–244.
Meinhart, C. D., Wereley, S. T. & Santiago, J. G. (2000). A PIV algorithm for estimating time-averaged velocity fields, *Journal of Fluids Engineering* **Vol. 122** (No. 2): 285–289.
Nakajima, K., Osa, A., Maekawa, T. & Miike, H. (1997). Evaluation of body motion by optical flow analysis, *Japanese Journal of Applied Physics* **Vol. 36** (No. 5A): 2929–2937.
Nakajima, Y., Inomata, H., Nogawa, H., Sato, Y., Tamura, S., Okazaki, K. & Torii, S. (2003). Physics-based flow estimation of fluids, *Pattern Recognition* **Vol. 36** (No. 5): 1203–1212.
Nomura, A., Miike, H. & Koga, K. (1991). Field theory approach for determining optical flow, *Pattern Recognition Letters* **Vol. 12** (No. 3): 183–190.
Press, W. H., Flannery, B. P., Teukolsky, S. A. & Vetterling, W. T. (1988). *Numerical Recipes in C: The Art of Scientific Computing*, Cambridge University Press, Cambridge, England.
Raffel, M., Willert, C. E., Wereley, S. T. & Kompenhans, J. (2007). *Particle Image Velocimetry: A Practical Guide*, Springer-Verlag, Berlin, Germany.
Roesgen, T. (2003). Optimal subpixel interpolation in particle image velocimetry, *Experiments in Fluids* **Vol. 35** (No. 3): 252–256.
Scarano, F. (2002). Iterative image deformation methods in PIV, *Measurement Science and Technology* **Vol. 13** (No. 1): R1–R19.
Sugii, Y., Nishio, S., Okuno T. & Okamoto, K. (2000). A highly accurate iterative PIV technique using a gradient method, *Measurement Science and Technology* **Vol. 11** (No. 12): 1666–1673.
Terzopoulos, D. (1986). Image analysis using multigrid relaxation methods, *IEEE Transactions on Pattern Analysis and Machine Intelligence* **Vol. PAMI–8** (No. 2): 129–139.
Theunissen, R., Scarano, F. & Riethmuller, M. L. (2010). Spatially adaptive PIV interrogation based on data ensemble, *Experiments in Fluids* **Vol. 48** (No. 5): 875–887.
Tokumaru, P. T. & Dimotakis, P. E. (1995). Image correlation velocimetry, *Experiments in Fluids* **Vol. 19** (No. 1): 1–15.
Westerweel, J., Dabiri, D. & Gharib, M. (1997). The effect of a discrete window offset on the accuracy of cross-correlation analysis of digital PIV recordings, *Experiments in Fluids* **Vol. 23** (No. 1): 20–28.
Willert, C. E. & Gharib, M. (1991). Digital particle image velocimetry, *Experiments in Fluids* **Vol. 10** (No. 4): 181–193.

Engineering the Future

Edited by Laszlo Dudas

ISBN 978-953-307-210-4
Hard cover, 414 pages
Publisher Sciyo
Published online 02, November, 2010
Published in print edition November, 2010

This book pilots the reader into the future. The first three chapters introduce new materials and material processing methods. Then five chapters present innovative new design directions and solutions. The main section of the book contains ten chapters organized around problems and methods of manufacturing and technology, from cutting process optimisation through maintenance and control to the Digital Factory. The last two chapters deal with information and energy, as the foundations of a prospering economy.

How to reference

In order to correctly reference this scholarly work, feel free to copy and paste the following:

Atsushi Nomura, Koichi Okada, Hidetoshi Miike and Hidemi Yamada (2010). Gradient-based Approach for Determination of Oscillating Flow Fields in PIV, Engineering the Future, Laszlo Dudas (Ed.), ISBN: 978-953-307-210-4, InTech, Available from: http://www.intechopen.com/books/engineering-the-future/gradient-based-approach-for-determination-of-oscillating-flow-fields-in-piv

INTECH
open science | open minds

InTech Europe
University Campus STeP Ri
Slavka Krautzeka 83/A
51000 Rijeka, Croatia
Phone: +385 (51) 770 447
Fax: +385 (51) 686 166
www.intechopen.com

InTech China
Unit 405, Office Block, Hotel Equatorial Shanghai
No.65, Yan An Road (West), Shanghai, 200040, China
中国上海市延安西路65号上海国际贵都大饭店办公楼405单元
Phone: +86-21-62489820
Fax: +86-21-62489821

IntechOpen